Nanoscale early oxidation mechanisms of model FeCrNi austenitic stainless steel surfaces at room temperature

Li Ma, Benjamin Lynch, Frédéric Wiame, Vincent Maurice, Philippe Marcus

Nanoscale early oxidation mechanisms of model FeCrNi austenitic stainless steel surfaces at room temperature

Li Ma[1,2,3], Benjamin Lynch[1], Frédéric Wiame[1*], Vincent Maurice[1*], Philippe Marcus[1*]

[1] *PSL Research University, CNRS-Chimie ParisTech, Institut de Recherche de Chimie Paris, Research Group Physical Chemistry of Surfaces, 75005 Paris, France*

[2] *Department of Materials Science, Fudan University, Shanghai, 200433, China*

[3] *Zhuhai Fudan Innovation Institute, Hengqin New Area, Zhuhai, 519000, China*

Abstract

Scanning tunneling microscopy was applied to investigate the topographical and structural alterations at small spatial and temporal scales of a model 304 austenitic stainless steel surface resulting from ultra-low exposures to gaseous oxygen at room temperature. The 2D nucleation and growth mechanisms were observed until surface saturation by a fully covering and nanogranular Cr(III)-enriched oxide film. Local supply of metallic Fe and Cr for oxide nucleation and growth is concluded to be at the origin of heterogeneity developed in the oxide film at the nanoscale. This work provides nanoscale understanding basis for composition and morphology tuning of Cr-enriched oxide film for improved local stability of passivity.

Keywords: stainless steel, initial oxidation mechanism, oxide film nanoscale morphology, scanning tunneling microscopy, single crystal

1. Introduction

The durability of stainless steels (SS), a class of metallic alloys widely used in both industry and everyday life, relies on a surface oxide film, the passive film, not exceeding

*Corresponding authors

Email addresses: frederic.wiame@chimieparistech.psl.eu (Frédéric Wiame[1]), vincent.maurice@chimieparistech.psl.eu (Vincent Maurice[1]), philippe.marcus@chimieparistech.psl.eu (Philippe Marcus[1])

Author preprint published in Corrosion Science *doi: 10.1016/j.corsci.2021.109653*

a few nanometers in thickness and forming a self-healing compact barrier that protects the substrate from degradation in corrosive environments. However, in chloride-containing environments, local breakdown of the passive film can occur, followed by the initiation of localized corrosion by pitting in the absence of self-healing, which can cause structural and aesthetic damage, and can endanger the environment and even lives.

A wealth of work has proved that the passive film enrichment in Cr oxide is a key aspect of the passivity of SS, owing to the higher chemical stability of this oxide compared to Fe oxides [1–6]. Nearly no Ni oxide enters the composition of the passive film on Ni-containing austenitic SS, and the initiation of localized corrosion by pitting can be combated with the addition of molybdenum at a few atomic percent level in the bulk alloy [7–13].

Recently, the understanding of the link between passivity breakdown by local failure at microscopic level and chemical/structural heterogeneities/defects in the passive film has motivated fundamental research at nanometric/atomic scales [14–17]. Nanoscale surface heterogeneities, including the Cr enrichment, would be the dominant factor limiting film stability. Thus, the initial oxidation stages, including oxygen adsorption and oxide nucleation and growth, by which the surface oxide film is pre-formed before passivation in a corrosive aqueous medium, and their role on the Cr enrichment are worthy of detailed and systematic investigations. Moreover, the corrosion resistance behavior could be improved by the control of surface heterogeneity at the nanoscale, which could be of benefit to practical applications. For example, the clean surface of FeCrNi alloy pre-oxidized in well-controlled conditions presented a more uniform and compact morphology at nanoscale in contact with water vapor. This compact Cr oxide barrier can prevent further oxidation of Fe [18].

The distribution of surface oxides can be examined by scanning tunneling microscopy (STM) at small spatial and temporal scales. A single-crystalline surface, of well-defined orientation, can be used in order to avoid the complexity brought by microstructure defects and dissimilar crystallographic orientations in polycrystals. Combined with the precise control of the interface between solid and gas, this approach provides the appropriate monitoring of the surface state and oxidation kinetics at nanometric/atomic scales. Compositional studies have been carried out on model single-crystal SS surfaces over the years [17, 19–22]. How-

ever, the endeavors to study detailed structural alterations of well-defined surfaces at high resolution in space and time are still limited [16, 23]. Our previous work [16, 17] addressed the initial oxidation mechanisms of a FeCrNi single-crystal surface at moderate temperature (250 °C) and revealed, at the nanoscale, the formation of well-organized oxide patterns and chemical/structural heterogeneities/defects originating from the different stages of the oxide film growth. STM investigation of early stage oxidation at lower temperature, i.e. at room temperature (RT), of the same surface should provide new insights into temperature effects for surface heterogeneity monitoring.

In this work, early stage oxidation was performed on a single-crystalline Fe-18Cr-13Ni(100) surface upon precise gaseous oxygen exposure up to saturation of the oxide growth. The oxide growth mechanisms were investigated by STM and X-ray photoelectron spectroscopy (XPS). The complementary XPS study of oxidation at different temperatures was reported previously [17]. The comparison of the early stage oxidation mechanisms at RT and higher temperatures allows us to discuss possible factors for tuning surface heterogeneity.

2. Material and methods

Experiments were performed in an ultra-high vacuum (UHV) system for surface preparation and analysis, with interconnected preparation, XPS and STM chambers. The base pressure in the UHV system was less than 10^{-10} mbar.

A (100)-oriented single-crystal of Fe-18Cr-13Ni (at.%) (99.999% purity) was used and the surface was prepared first by mechanical and electrochemical polishing outside the UHV system [19]. Then, preparation cycles – Ar^+ ion sputtering (1 kV, 10 μA, 10 minutes) and annealing (700 °C, 10 minutes) – were carried out in the UHV preparation chamber in order to obtain an oxide-free and well-structured surface. Surface cleanness and structure, forming the characteristic $(\sqrt{2} \times \sqrt{2})$R45° reconstructed superstructure [24], were examined by XPS and low-energy electron diffraction (LEED), respectively.

Gaseous oxygen inlet was controlled by a precision valve, keeping the pressure under 10^{-6} mbar. In this range of pressure no difference was observed on oxidation kinetics as a function of exposure. Exposure to oxygen was accurately calculated by integration of the

oxygen pressure recorded as a function of exposure time. XPS was used in snapshot mode in order to measure the oxygen uptake during the ongoing oxidation by recording the O 1s core level spectrum every 10 seconds, which enhances the continuous monitoring of the surface composition variation. Ultra-low exposures, in the 0−15 L range (1 langmuir = 1.33×10^{-6} mbar·s, 1 L corresponds approximately to an exposure of one atom of oxygen by surface atom), selected from the oxygen uptake curve, were carried out, and XPS and STM were performed to investigate the chemical and structural alterations caused by the oxide nucleation and growth mechanisms at RT, respectively.

XPS analysis was performed with an Argus spectrometer using the monochromated XM1000 MkII Al Kα source (1486.6 eV), both from Scienta Omicron. Survey and high-resolution spectra of core levels were recorded with constant pass energy of 50 eV and 20 eV, respectively. XPS spectra were measured at take-off angles of the photoelectrons of 45° and 90°. They were treated with the CasaXPS software [25]. The adopted accurate spectral decomposition methodology and the results obtained for oxidation at different temperatures, RT, 150°C and 250 °C, were discussed in detail in our previous study [17].

STM experiments were conducted with a VT STM XA, also from Scienta Omicron. Tungsten tips, electrochemically etched in NaOH aqueous solution, were used and further prepared under UHV by heating, voltage pulses and high voltage scanning. STM images were obtained in constant current mode and corrected from the lateral drift and from the slope of the terraces using the SPIP software [26]. The bulk parameter of 0.359 nm of the *fcc* lattice of the Fe-Cr-Ni alloy was taken as reference to calibrate the atomically resolved images. Brightness, contrast and saturation of images were adjusted to improve the image quality and to enhance local details of interest. No image filtering was applied.

3. Results

3.1. XPS characterization

The oxygen uptake of the Fe-18Cr-13Ni(100) surface measured by *in situ* XPS at RT is shown in Figure 1. The snapshot image of the variation of the O 1s spectrum *vs* oxygen

exposure is presented in Figure 1 (a). O_2 was first dosed at a pressure of 8×10^{-9} mbar to gain a slow rate of surface evolution, and then augmented to 10^{-8} mbar, 10^{-7} mbar and 10^{-6} mbar in order to observe the influence of oxygen partial pressure on oxidation rate (Figure 1 (b)). The integration of recorded oxygen pressure with exposure time, i.e. the area under the curve in (b), shows that 460 L of oxygen was introduced after 5000 s of exposure (Figure 1 (c)). The normalized intensity of the O 1s peak increases rapidly at first with increasing exposure to oxygen. The insert in (c) details the kinetics of oxidation for the exposure limited to 15 L. It can be observed that a plateau occurs at 8−12 L, and thus that the oxygen uptake reaches saturation after exposure to about 10 L at RT. Moreover, the increase of the oxygen pressure up to 10^{-6} mbar after saturation does not change the uptake level at saturation.

Based on the oxygen uptake curve measured at RT, high-resolution XPS spectra of the Cr 2p, Fe 2p, Ni 2p, O 1s and N 1s core levels were recorded for exposures of 0.5 L, 3.1 L, 5.9 L and 13.9 L, respectively, in order to analyze the evolution of the surface composition. In our previous work [17], we discussed in detail the decomposition methodology, the extracted peak components and their assignment, as well as the evolution of the surface composition as a function of exposure at RT, 150 °C and 250 °C. Here, we compile in Table 1 the relative atomic concentrations for the Fe (Fe^0 and $Fe^{2+/3+}$), Cr (Cr^0, Cr^{3+} and Cr-N bonding), Ni (Ni^0), oxygen and nitrogen species measured at 45° and 90° take-off angles after exposure in the 0−15 L range at RT. No oxidized Ni (Ni^{2+}) was detected after oxidation since only the metallic component of the Ni $2p_{3/2}$ and $2p_{1/2}$ spin-orbit doublet was measured at binding energies of 852.8 eV and 870.1 eV, respectively, in agreement with previous studies [19, 20, 27]. Although N species disappeared after ion sputtering, a component indicative of Cr-N bonding was identified on the oxide-free surface as a result of N co-segregation with Cr from the sub-surface region induced by annealing during surface preparation [17].

Figure 2 shows separately the variations of the relative concentration of Fe^0, Cr^0 and Ni^0 metallic states and $Fe^{2+/3+}$ and Cr^{3+} oxidized states for very early stages of exposure, at 45° and 90° take-off angles. The variations for exposures up to 460 L at 45° take-off angle were discussed in a previous paper [17]. The initial oxide-free surface is enriched in

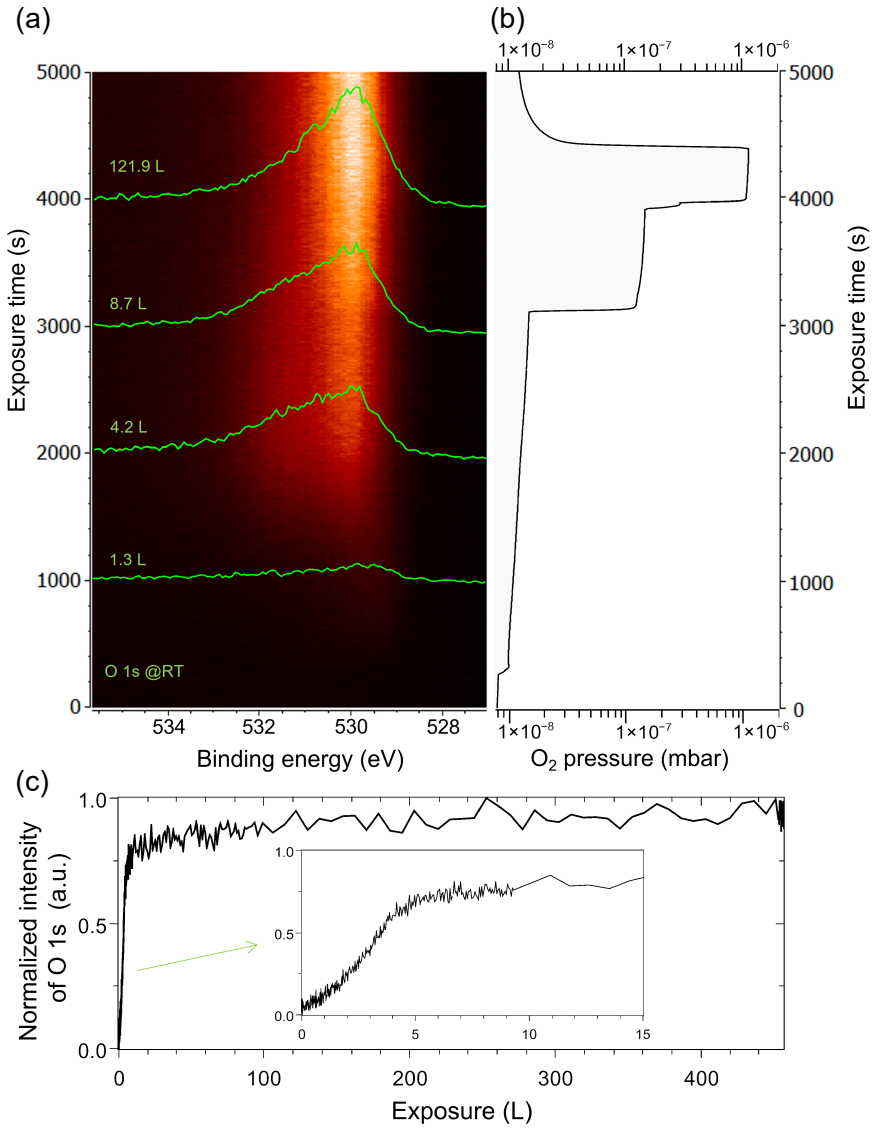

Figure 1: Oxygen uptake for the Fe-18Cr-13Ni(100) surface exposed to gaseous oxygen at RT. (a) Snapshot image of the evolution of the XPS O 1s spectrum upon exposure to gaseous oxygen for 0−5000 s at RT. The brightness shows the peak intensity. The inserted lines present the spectra for exposure times of 1000 s (1.3 L), 2000 s (4.2 L), 3000 s (8.7 L) and 4000 s (121.9 L). (b) Evolution of O_2 pressure (10^{-8} to 10^{-6} mbar) during exposure. (c) Oxygen uptake as a function of exposure calculated from (b). The insert enlarges the 0−15 L (0−3200 s) exposure range.

Table 1: Relative atomic concentrations of the Fe, Cr, Ni, O and N components for the Fe-18Cr-13Ni(100) surface exposed to gaseous oxygen at RT. Fe% + Cr% + Ni% + O% + N% = 100%, with uncertainty of 1%. θ − take-off angle (°); Exp − oxygen exposure (L).

θ (°)	Exp (L)	Relative concentration (at.%)									
		Fe 2p	Fe^0	$Fe^{2+/3+}$	**Cr 2p**	Cr^0	$Cr^{3+}{}_{ox}$	Cr-N	**Ni 2p**	**O 1s**	**N 1s**
45°	0	**53.9**	53.9	0.0	**28.8**	28.4	0.0	0.4	**8.4**	**0.0**	**8.9**
	0.5	**45.3**	41.1	4.2	**34.1**	33.2	0.2	0.7	**5.7**	**3.7**	**11.3**
	3.1	**51.5**	44.6	6.9	**22.6**	17.4	3.5	1.8	**6.6**	**14.2**	**5.1**
	5.9	**35.0**	27.6	7.4	**21.7**	7.8	10.5	3.4	**5.0**	**34.7**	**3.7**
	13.9	**34.5**	26.1	8.4	**21.1**	7.0	10.6	3.5	**4.6**	**36.1**	**3.7**
90°	0	**56.0**	56.0	0.0	**29.6**	29.3	0.0	0.2	**8.1**	**0.0**	**5.7**
	0.5	**56.8**	52.9	3.7	**28.8**	28.5	0.0	0.3	**6.5**	**1.9**	**6.0**
	3.1	**51.1**	46.1	5.0	**23.0**	18.9	2.3	1.7	**6.9**	**14.4**	**4.6**
	5.9	**40.1**	33.8	6.3	**22.5**	9.9	9.5	3.1	**5.9**	**28.3**	**3.3**
	13.9	**39.8**	32.7	7.1	**21.1**	8.7	9.3	3.1	**5.3**	**30.6**	**3.2**

metallic Cr^0 at a concentration (31 at.% of the metallic elements) superior to the nominal percentage of 18 at.%, which we assign to the effect of repeated surface annealing prior to the oxidation experiments. For the take-off angle of 45° (Figure 2 (a) and (b)), the Cr^{3+} oxide species increase with oxygen exposure reaching 5%, 34%, 59% and 56% of the oxidized species after 0.5 L, 3.1 L, 5.9 L and 13.9 L, respectively. This trend, also observed at 90° take-off angle, shows that more Fe oxidizes until about 5 L, after which the oxidation of Cr becomes predominant until saturation of the oxide growth. The progressive establishment of the regime of dominant Cr oxidation is supported by the progressive decrease of the concentration in metallic Cr^0 reaching 19% of the metallic elements at saturation (Figure 2 (b)), while the concentrations in metallic Fe^0 and Ni^0 reach 69 and 12 at.%, respectively. The Cr-N component increases with exposure, showing a similar evolution to that of Cr^{3+} oxide species (Table 1).

For the take-off angle of 90° (Figure 2 (c) and (d)), i.e. for a deeper region detected underneath the topmost surface, the metallic components have almost the same relative

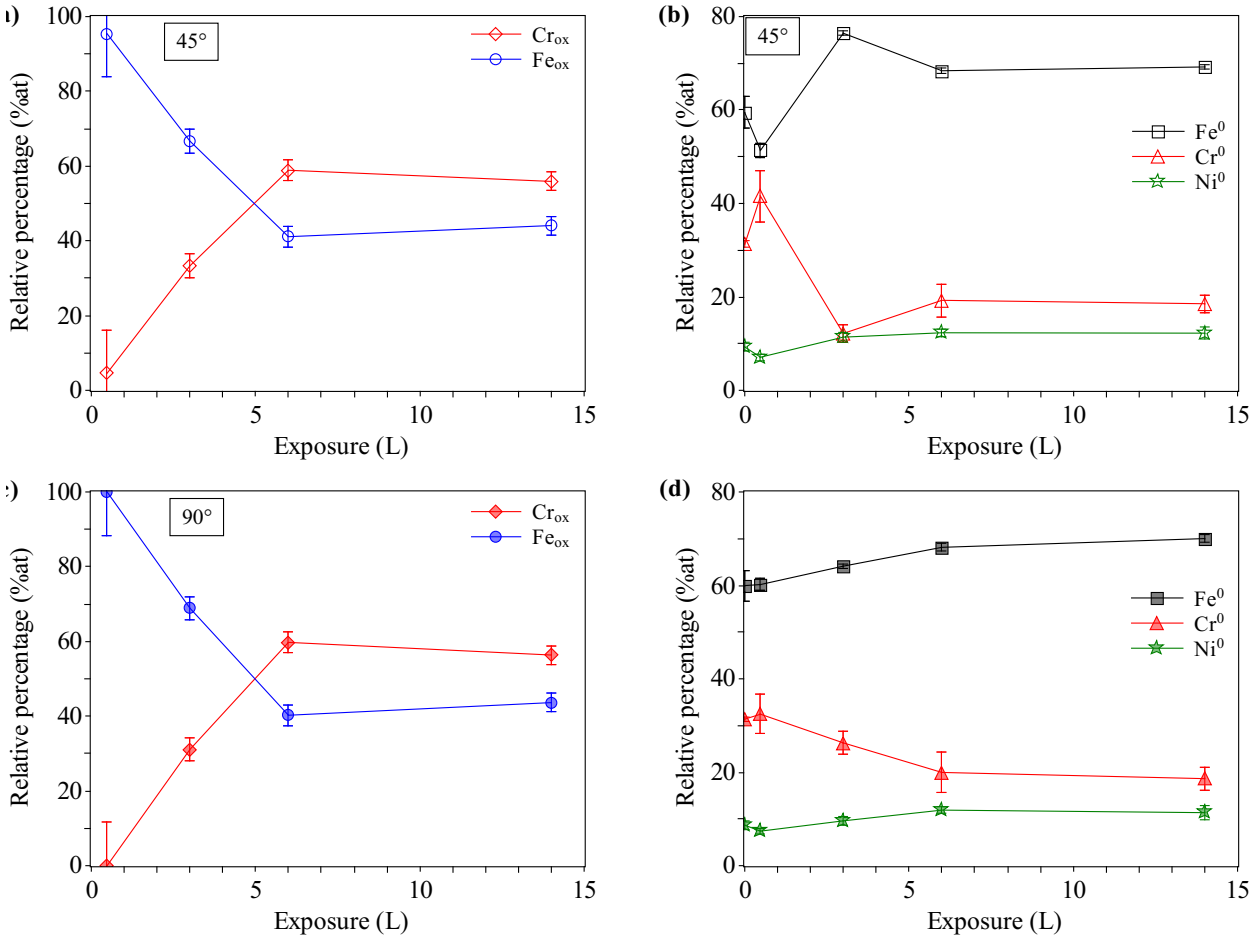

Figure 2: Variation of the relative concentrations of Fe, Cr and Ni compounds in metal and oxide phases with increasing exposure to oxygen at RT. The total percentage of metallic or oxide compounds is equal to 100 at.%. (a)(b) Take-off angle 45°; (c)(d) Take-off angle 90°. The error bars correspond to the uncertainties associated with the fitting parameters of the XPS spectra decomposition.

concentration (70%Fe-19%Cr-11%Ni *vs.* 69%Fe-19%Cr-12%Ni at take-off angle of 45°) after saturation to oxygen, indicating homogeneous in-depth distribution in the modified alloy region underneath the oxide film after growth at saturation. After 0.5 L exposure, the Cr^{3+} oxide concentration is under the detection limit (assigned to 0%), while it is only slightly different compared to 45° after saturation to oxygen. After 3.1 L, preferential consumption of Cr^0 metal from the modified alloy region for Cr^{3+} oxide formation at the surface is confirmed by a lower concentration decrease measured at 90° than at 45° take-off angle.

Thus, before reaching surface saturation to oxygen at RT, Cr^{3+} and $Fe^{2+/3+}$ oxide nuclei

are competitively formed by direct oxidation of Cr^0 and Fe^0 at the outermost surface. Fe oxide nucleation started at very low oxygen exposure, whereas the oxide nucleation of Cr, which is thermodynamically more stable, was delayed. After the initial oxidation of Fe^0, Cr^0 accumulated in the surface as a result of segregation (and co-segregation of N) induced by repeated annealing, contributes to balance $Fe^{2+/3+}$ formation and to sustain predominant Cr^{3+} formation until growth at saturation of the oxide film, as supported by the alloy composition underneath the oxide film reaching values close to the nominal bulk composition. At RT, further oxide growth is limited due to slow diffusion, unlike at 150°C and 250 °C for which larger oxygen uptakes were observed [17].

Figure 3 shows the evolution of the line shape of the high-resolution O 1s spectra with oxygen exposure. The main peak, located first at 529.8 eV (at 0.5 L) and then at 530.2 eV (from 3.1 L on), is assigned to the O^{2-} ions from the matrix of the oxide. The shoulder peak located at 531.4 eV is assigned to O^{2-} or O^- ions compensating the defects in the subsurface (dislocations, vacancies) and the shoulder located between 532 eV and 533 eV is assigned to adsorbed O_2. This oxygen peak designation is in agreement with the literature [28]. Comparison of the line shapes between RT, 150°C and 250 °C experiments shows that the shoulders associated with O^- and adsorbed O_2 species are more pronounced at RT, with more oxygen captured after 3.1 and 5.9 L exposures at RT (see supporting information in [17]), meaning that oxygen adsorption is favored for exposures less than 10 L at RT. As discussed above, Fe oxide is mainly nucleated at 0.5 L after which the growing surface oxide nuclei become increasingly enriched in Cr. The main oxide component at 529.8 eV for 0.5 L exposure can thus be attributed to O^{2-} ions essentially in Fe oxide nuclei whereas the shift to 530.2 eV for higher exposure would correspond to the formation of a mixed Fe and Cr oxide nuclei increasingly enriched in Cr.

Noticeably, more Fe oxide nuclei were formed at 0.5 and 3.1 L at RT than at 150°C and 250 °C for which the formation of Cr oxide was already predominant [17]. We propose the following explanation for this temperature effect. The Fe atoms located in the topmost surface plane would interact directly with oxygen, whereas the reactivity of the Cr atoms would be poisoned and thus delayed by their interaction with nitrogen (segregated at the

surface during surface preparation). Due to the relative lower temperature, there would be limited diffusion channel of Cr from subsurface. Activation energy for displacing nitrogen bonded to Cr is also likely a major factor explaining the observed temperature effect. As soon as the Cr mobility is sufficient as a result of surface defects created during Fe oxide nucleation, the oxidation of Cr gradually takes over the reaction. Thus, at RT, in the presence of surface nitrogen, Fe oxide nuclei form first and it is only after 3.1 L exposure that the kinetic barrier for Cr oxide nucleation would be overcome and that Cr^{3+} preferentially forms due to the higher Cr oxide thermodynamic stability. Whereas, at 150 °C and 250 °C, this initial kinetic barrier for Cr oxidation is overcome faster by thermal activation with the preferential nucleation of Cr^{3+} oxide. The preferential formation of Cr^{3+} oxide is sustained by the initial Cr^{0} enrichment in the sub-surface atomic planes until growth of the oxide film at saturation, with thinner oxide film formed at RT than at 150 °C and 250 °C due to limited atomic mobility.

3.2. STM characterization

Figure 4 (a) shows a typical STM image of initial oxide-free Fe-18Cr-13Ni(100) surface. The topography alternates terraces and atomic multi-steps. On the terraces, chemical contrast is observed at the atomic scale and the atomic lattice displays a $(\sqrt{2} \times \sqrt{2})R45°$ superstructure (Figure 4 (b)). It includes vacancy defect lines, constituted of two missing atom rows and periodically distributed along the [010] direction. This characteristic superstructure of the oxide-free surface has been previously discussed in detail [24]. The step borders in the immediate vicinity of the step edges were identified as the preferential site of accumulation of the Cr-N species co-segregated upon annealing during surface preparation [17, 24].

Figure 5 shows the surface after an oxygen exposure of 0.48 L at RT. The surface sustains its terrace and multi-steps topography as well as the initial superstructure and vacancy lines on the terraces. At the multi-steps, only dispersed protrusions assigned to oxide nuclei are detected, unlike after oxide nucleation at 250 °C for which the multi-steps were saturated with nuclei assigned to Cr^{3+} oxide [16, 17]. At RT, the quality of the STM images was de-

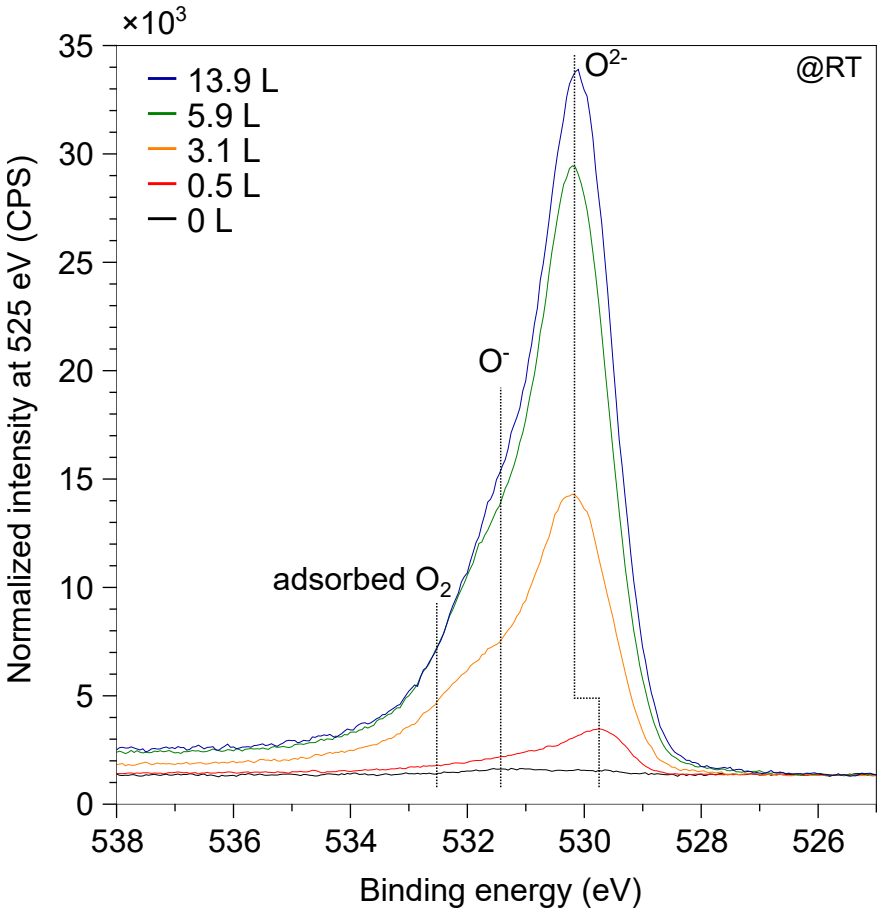

Figure 3: XPS O 1s core level spectra measured for the Fe-18Cr-13Ni(100) surface exposed to oxygen from 0 to 14 L at RT. Take-off angle is 90°.

graded, possibly by the presence of more oxygen physically adsorbed. However, the absence of saturation of the multi-steps by oxide nuclei was confirmed at higher exposure. On the terraces, protrusions, marked by ovals in Figure 5, are observed, with an apparent height of about 40−50 pm, and a size of about 0.5 nm in diameter. These protrusions are assigned to nuclei of (essentially) Fe oxide formed at an exposure of 0.5 L. They may also include adsorbed oxygen atoms. Due to STM tip size convolution and electronic effects, the number of metal atoms in these nuclei can only be roughly estimated to between 3 and 10. The density of nuclei is estimated to 0.03 ± 0.02 nm^{-2}. These oxide nuclei are preferentially formed close to the initial vacancy defect lines. Indeed, as observed in Figure 5 (a), about 1/2 of them are located in the vacancy lines, 1/4 in the vicinity of the vacancy lines (within a distance

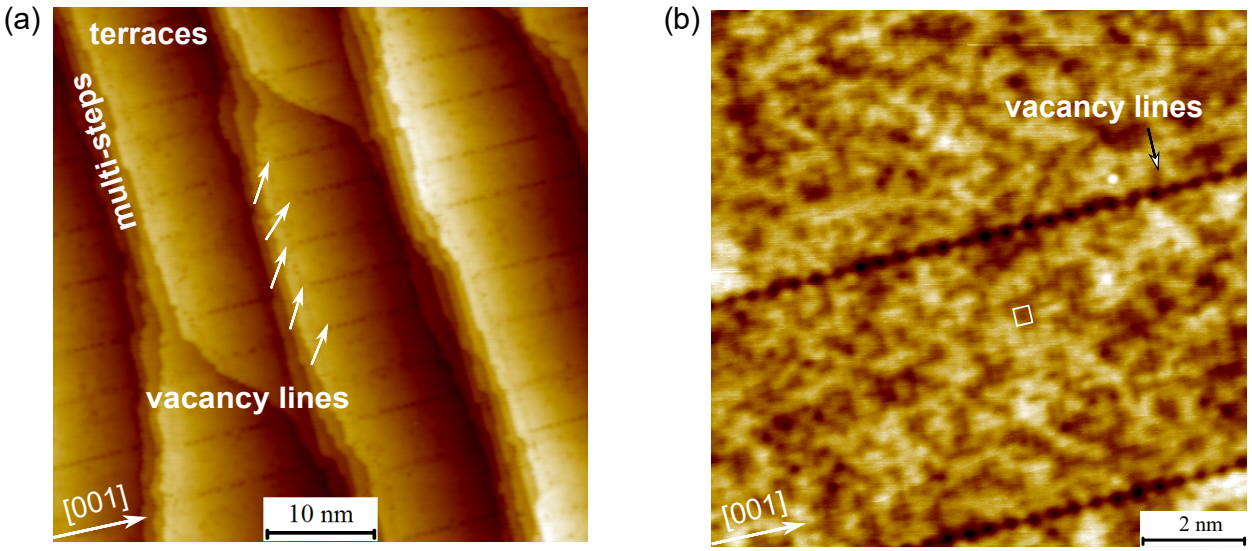

Figure 4: Initial oxide-free Fe-18Cr-13Ni(100) surface. (a) STM image of the terraces and multi-steps morphology, 50 nm×50 nm, $I = 0.5$ nA, $V = -0.5$ V (b) STM image highlighting the atomic network and vacancy lines on the terraces, 10 nm×10 nm, $I = 0.5$ nA, $V = 0.5$ V. Unit cell of atomic lattice is marked by a white square in (b).

of 1 nm) and the last 1/4 on the terrace centers. The vacancy lines are altered by the oxide nuclei. For example, the site occupation is observed and new vacancies are created. Thus, terrace atoms, presumably Fe as inferred from the XPS data, from the topmost atomic plane would become the oxide nucleation sites and the formation of the nuclei would leave atomic vacancies around.

Figure 6 shows the surface after an oxygen exposure of 0.91 L at RT. The initial topography characterized by alternation of terraces and multi-steps persists (Figure 6 (a)). Multi-steps are fuzzy and it is difficult to identify their atomic edges. However, no saturation by patterns that could be associated with oxide nucleation are observed at the multi-steps like it was after 0.96 L exposure at 250 °C [16, 24]. On the terraces, the periodic lines of vacancies can still be observed (Figure 6 (a)), as well as the initial $(\sqrt{2} \times \sqrt{2})$R45° lattice of the topmost plane (Figure 6 (b) and (c)). Oxide nuclei are observed on the terraces (Figure 6 (c)), with apparent height of about 40−60 pm and a size of about 0.5 nm×1.0 nm, close to those measured at 0.5 L. They are assigned to Fe oxide, possibly mixing more Cr

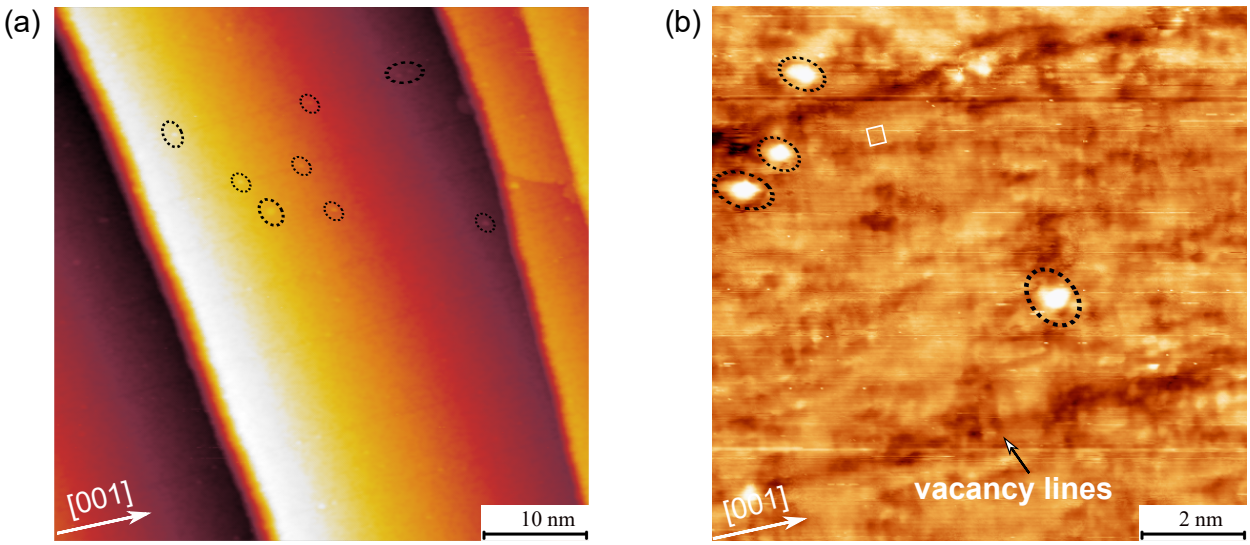

Figure 5: Initial oxide nucleation after an oxygen exposure of 0.48 L at RT. (a) STM image of terraces and multi-steps topography, 50 nm×50 nm, $I = 0.5$ nA, $V = 0.5$ V. (b) STM image of terrace highlighting the site of adsorbed oxygen or oxide nuclei on terraces, 10 nm×10 nm, $I = 4.0$ nA, $V = 0.3$ V. Unit cell of atomic lattice is marked by a white square in (b). Ovals mark oxide nuclei in (b).

according to the composition trend observed after the 0.5 L exposure (Figure 2, Table 1). No significant increase of the density of oxide nuclei was observed. However, more vacancies are observed in the topmost atomic plane due to consumption of (presumably Fe) atoms, as evidenced by the new dark sites appearing on the terraces and forming no well-defined pattern (Figure 6 (b)). These new vacancies are preferentially linked to the initial vacancy defect lines where oxide nuclei are formed, suggesting that their formation is related to the growth of the oxide nuclei. As a result of the formation of oxide nuclei, the initial vacancy defect lines are divided into segments of vacancies and become less distinct (Figure 6 (c)).

Figure 7 shows the surface morphology after an oxygen exposure of 2.98 L at RT. The initial substrate topography is still observed (Figure 7 (a)). The multi-steps are persistent but are now covered by oxide nuclei, showing delayed nucleation in these sites compared with oxidation at 250 °C. According to the composition trend observed by XPS (Figure 2, Table 1), these nuclei can be assigned to (mostly) Cr^{3+} oxide. Their delayed nucleation would result from the kinetic barrier effect of the Cr-N component initially accumulated at the multi-steps. In Figure 7 (b), the slope of the terraces in Figure 7 (a) was leveled and

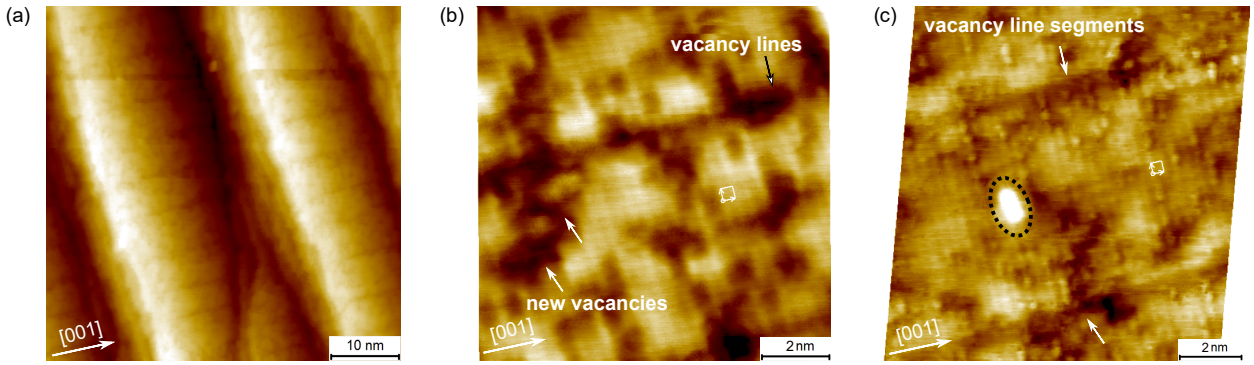

Figure 6: Initial oxide nucleation after an oxygen exposure of 0.91 L at RT. (a) STM image of terraces and multi-steps topography, 50 nm×50 nm, $I = 5.0$ nA, $V = -0.5$ V. (b) STM image of terrace highlighting atomic network, vacancy defect lines and newly formed vacancies, 10 nm×10 nm, $I = 5.0$ nA, $V = -0.5$ V. (c) STM image of terrace highlighting oxide nucleation (marked by oval) and vacancy line segmentation, 11 nm×11 nm, $I = 5.0$ nA, $V = -0.5$ V. Unit cell of topmost atomic network is marked by squares in (b) and (c).

adjusted to the same topographic height for all terraces in order to improve the contrast. The oxide nuclei on the terraces have an apparent height of 80−140 pm. They form at terrace borders (Figure 7 (c)), in the vicinity of step edges (within a distance of 1−2 nm), as well as in the terrace centers, near the initial vacancy defect lines (Figure 7 (d)). The size and the density of the oxide nuclei increased, in agreement with the oxygen uptake curve that showed an increased oxidation rate at about 3 L (Figure 1 (c)). The nuclei have a diameter of about 1.5 nm for the most part, but can reach 2.1 nm. According to the composition trend measured by XPS, these nuclei formed on the terraces could mix Fe and Cr oxide species, and be individually more enriched in Fe or Cr depending on the local supply of the metallic element.

The leveled terraces no longer show the typical structure characteristic of the oxide-free surface. The initial vacancy defect lines, or more accurately their remaining segments, are much less distinct and nearly vanished (Figure 7 (b)). New vacancies, forming short, dark lines oriented principally along the ⟨001⟩ directions, appear in the terraces center (Figure 7 (d)). These new short lines are assigned to the vacancy pathway left by atom diffusion in the topmost plane, mainly as a result of metals consumption for formation of the oxide

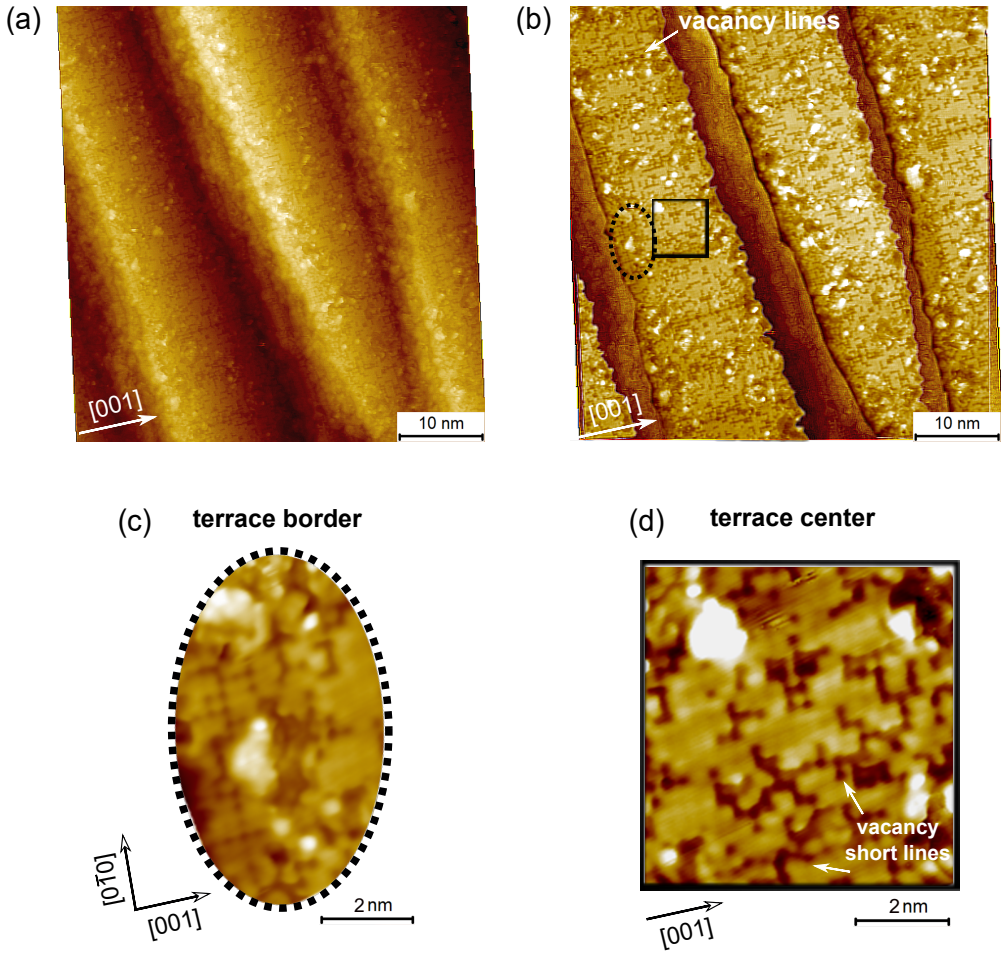

Figure 7: Initial oxide nucleation after an oxygen exposure of 2.98 L at RT. (a) STM image with oxide nucleation at terraces and multi-steps, 50 nm×50 nm, $I = 0.2$ nA, $V = -0.7$ V. (b) Terrace-leveled image of (a) highlighting the contrasted new vacancy patterns and oxide nuclei formed on the terraces. (c) Atomic structure at the terrace border in the domain marked in a dashed oval in (b), $I = 0.2$ nA, $V = -0.7$ V. (d) Atomic structure at the terrace center in the domain marked by a square in (b), $I = 0.2$ nA, $V = -0.7$ V.

nuclei. Figure 7 (c) also shows the reconstruction of terrace border in the vicinity of a step edge and where Cr-N were previously accumulated.

Figures 8 (a) and (b) show the surface morphology after oxygen exposures of 5.97 L and 9.08 L at RT, respectively. Oxygen saturation of the surface is nearly attained after an exposure of about 6 L, as evidenced in Figure 1 (c). The two images obtained for these two exposures present similar terraces and multi-steps topographies fully covered by surface oxide nuclei, in agreement with the near saturation of the oxygen uptake measured by XPS.

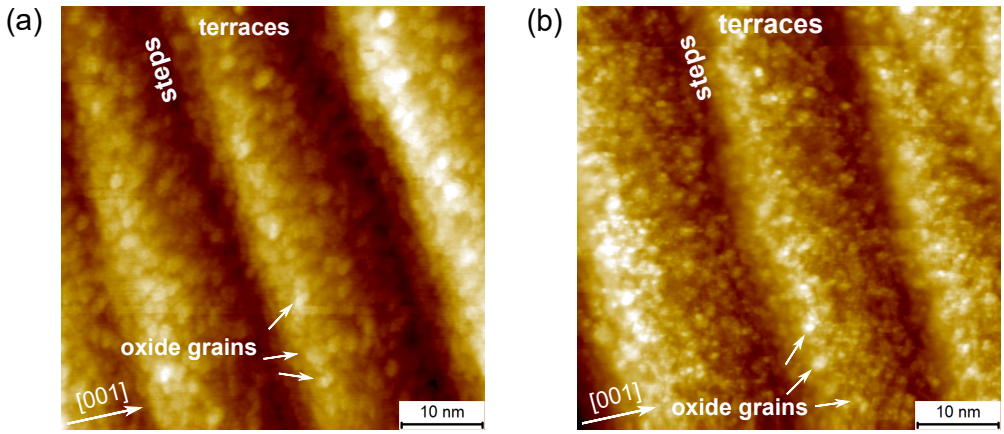

Figure 8: Oxide growth at saturation fully covering the terraces and multi-steps topography. (a) STM image after an oxygen exposure of 5.97 L at RT, 50 nm×50 nm, $I = 0.2$ nA, $V = -0.7$ V. (b) Image STM after an oxygen exposure of 9.08 L at RT. 50 nm×50 nm, $I = 0.2$ nA, $V = 1.5$ V.

The atomic edges of the multi-steps as well as the typical terrace structure of the oxide-free surface, including the $(\sqrt{2} \times \sqrt{2})$R45° superstructure and vacancy defect lines, are no longer observed. The grown oxide films are granular. On the terraces, the measured apparent height of the oxide nuclei is 0.3−0.6 nm, more than after shorter exposure and indicating the growth in thickness of the oxide nuclei. Average size of oxide nuclei is about 2−3 nm, indicating the lateral growth of the oxide nuclei and their possible coalescence.

At RT, the relative concentration of Fe and Cr oxide species remains almost invariant for exposures larger than 6 L (Figure 2, Table 1). At 250 °C, the relative concentration of Fe^{3+} exceeds that of Cr^{3+} for exposures larger than 30 L, with the continuous growth in thickness of the oxide film fed by Fe atomic transport from the sub-surface depleted in metallic Cr [16, 24]. However, at RT, Fe atomic transport from the alloy substrate is limited and cannot sustain further growth of the oxide thickness, like observed at higher temperatures. Thus, it is likely that the oxide films formed at exposures larger than 6 L at RT have globally similar composition, but consist of oxide nuclei that may be more enriched in Cr or Fe depending on the site of nucleation of the oxide nuclei and local supply of the metallic elements. Fe atom mobility has less effect on the oxide film stratification than at 250°C.

4. Discussion

Figure 9 presents an overview of the STM images depicting the early oxidation scenario measured on the Fe-Cr-Ni(100) surface at RT, starting from the oxide-free state and following exposures of 0.91 L, 2.98 L and 9.08 L to pure gaseous oxygen. According to the events observed for increasing exposure, the oxidation mechanism of stainless steel at RT is sequenced as follows: initial oxide nucleation for exposures lower than 3 L, delayed oxide nucleation, lateral growth and possible coalescence of the oxide nuclei in the 3−6 L range, and surface saturation by oxide nanograins for exposures beyond 6 L, an equivalent exposure of a few nanoseconds at atmospheric pressure.

In the initial nucleation stage (figures 5, 6 and 9b), compositional heterogeneity of the surface is generated at the nanometric scale from the hindered formation of Cr oxide grains due to nitrogen and limited atomic mobility, and thus favored Fe oxide nucleation at the very low exposures (< 3 L). Steps and defect lines on the terraces are the preferential sites for Fe oxide nucleation. The thermodynamically favored formation of Cr oxide is kinetically hindered by the Cr-N bonding generated by the surface preparation of the oxide-free surface. In contrast, at higher temperature (250 °C), thermal activation overcomes the N inhibiting effect by promoting Cr-N bond breaking, resulting in the expected preferential formation of Cr oxide. Surface defects, such as atomic vacancies and short vacancy lines created by Fe oxide nucleation, provided the diffusion passage of Cr atoms to trigger and sustain the oxidation of Cr. Initial nucleation of the Cr^{3+}-rich oxide occurs at the multi-steps for the most part, where Cr-N bonding was accumulated on the initial oxide-free surface.

Upon exposure to 3 L at RT (figure 7 and 9c), the oxide nuclei formed on the terraces become denser owing to continued nucleation and growth in height and in size, possibly involving coalescence. The oxide protrusions, formed at upper terrace borders and at the multi-steps, are considered as Cr^{3+}-rich oxide particles whose nucleation was delayed by N poisoning. According to the XPS kinetic results, the oxidation rate is the fastest at 3 L [17], which would result from the increase of the density of reacting metallic atoms in the topmost atomic layer because of the vanishing N kinetic barrier effect due to breakdown of

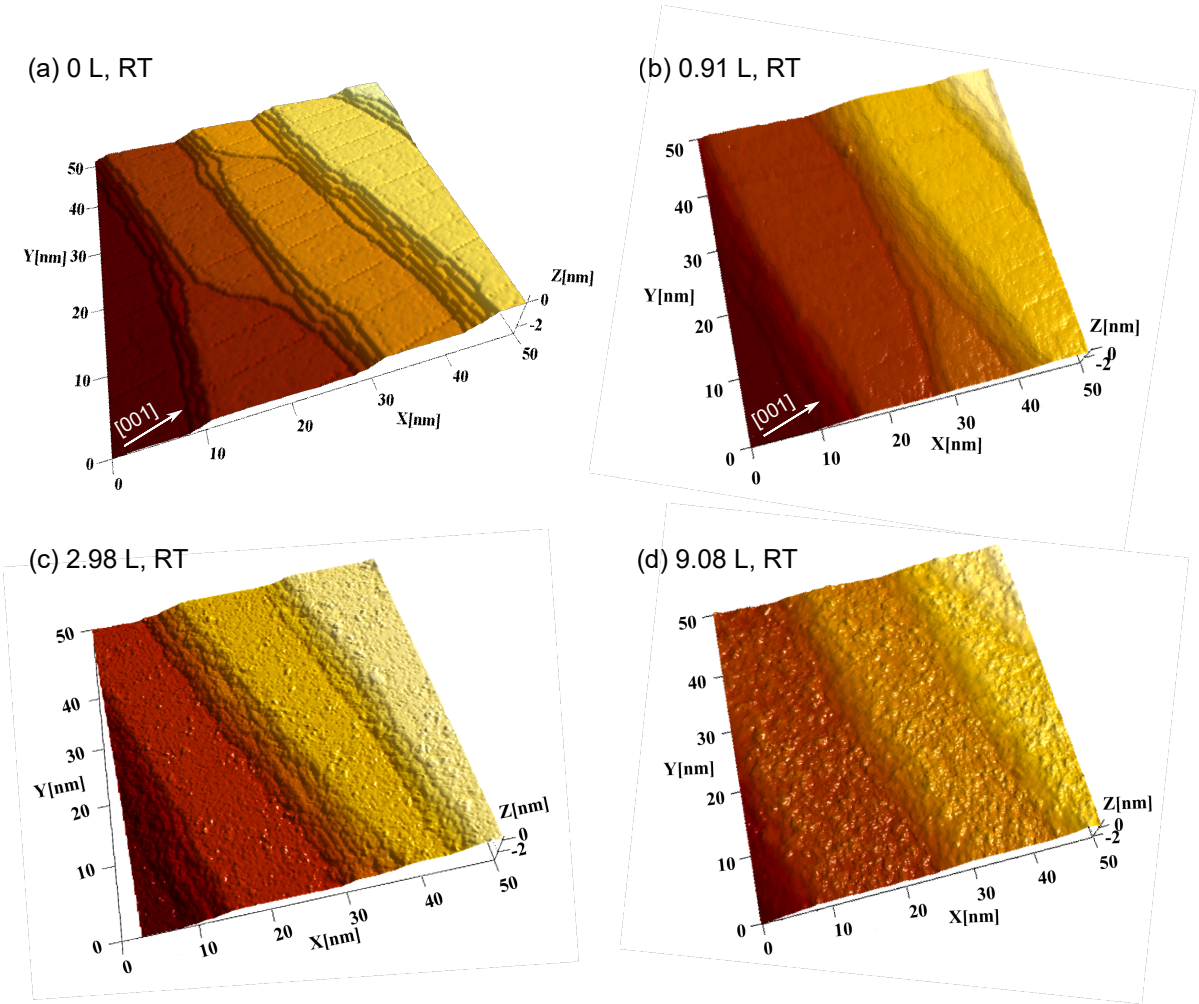

Figure 9: Overview of oxidation scenario for the Fe-18Cr-13Ni(100) surface exposed to gaseous oxygen at RT as observed by STM imaging. (a) oxide-free surface, $I = 0.5$ nA, $V = -0.5$ V; (b) oxide nucleation on terraces after 0.91 L, $I = 5.0$ nA, $V = -0.5$ V (nuclei visible in the zoom of Figure 6); (c) continuing nucleation on terraces and delayed nucleation on multi-steps after 2.98 L, $I = 0.2$ nA, $V = -0.7$ V; (d) saturation by oxide grains after 9.08 L, $I = 0.2$ nA, $V = 1.5$ V. Images of 50 nm×50 nm.

Cr-N bonding as suggested above. The new created vacancies at the topmost layer could contribute to the diffusion channel of Cr atoms and oxygen atoms into subsurface (observed at 250 °C). For exposures higher than 3 L (figure 8 and 9d), the oxide particles continue to nucleate, and grow in width and in height, most likely by coalescence, until progressively reaching the saturation of the surface by the oxide nanograins.

The surface oxide film grown at saturation at RT in the present work is not well structured as the oxide particles formed locally in the nucleation stage. This is also in contrast with the surface oxide formed at 250 °C that develops ordered structures. At 250 °C, the Cr^{3+}-rich oxide nuclei formed at the multi-steps and on the terraces are square-shaped and periodically arranged, at least locally, and the oxide film formed at surface saturation is crystalline with a Cr^{3+}-rich inner layer [16]. We can thus deduce that an elevated oxidation temperature reduces the physically adsorbed oxygen as shown by XPS [17] and accelerates the atomic mobility to the benefit of the formation of structural patterns in the nucleation stage as well as at surface saturation [16]. The formation of Cr^{3+}-rich structures benefits from the thermally-assisted supply of metallic Cr from the sub-surface region underneath the growing oxide (depth of 2−3 nm), however eventually leading to metallic Cr depletion. At RT, Fe oxidation dominates the surface reaction initially because of the poisoning effect of N-bonding on the oxidation of Cr. However, atomic mobility is limited in the topmost plane as well as atomic supply from the sub-surface, resulting in an island morphology of Fe-rich oxide particles in the initial nucleation stage and in a nanogranular morphology of (possibly mixed) Cr and Fe particles at saturation of the surface. At RT, limited atomic mobility and limited Cr supply from the sub-surface prevents the formation of a crystalline Cr^{3+}-rich inner layer of the surface oxide film.

At 250 °C, multi-layered oxide films are formed beyond surface saturation with preferential 3D growth of Fe oxide governed by the imperfections in the crystalline Cr^{3+}-rich inner layer and resulting in relatively inhomogeneous distribution of the oxides [16]. At RT, 3D growth after surface saturation is limited by atomic mobility, thus reducing the formation of Fe oxides at the outer surface and their inhomogeneous oxides distribution. The granular oxide film morphology obtained at RT indicates a finer nanoscale heterogeneity than at 250 °C, more dependent on the local supply of Cr and Fe for oxide nucleation and lateral growth because limited by atomic mobility. A Cr^{3+}-enriched oxide film is formed at saturation at RT.

We deduce from the oxidation mechanisms observed at different temperatures that the formation and 3D growth of Fe-rich oxide species gradually govern the heterogeneity of

the surface oxide at a higher temperature, while a thinner and more uniform oxide film is formed at RT and remains Cr-enriched for exposures beyond saturation. It is speculated that heating can facilitate the accommodation of the lattice mismatch between oxides and substrate and make the Cr-enriched oxide film more compact and structured. Therefore, a preparation method including oxidation at RT followed by annealing treatment may be beneficial to the compactness of Cr-enriched surface oxide layer, which could promote the homogeneous formation of Fe oxides at the outermost surface, avoiding the heterogeneities caused by the formation of protuberant Fe-enriched oxide islands (although minor Fe oxide nuclei persist).

Compared to the native film formed in air on the same stainless steel sample [11, 18], the oxidized surface obtained in the present work after saturation at RT at ultra-low pressure also sustains the substrate terrace and steps morphology but consists of more compact and smaller oxide grains. The native oxide film is rougher and more porous because Fe oxide species form at the outer surface in contact with water vapor. Therefore, pre-oxidation in gaseous oxygen environment is suggested as a beneficial pretreatment for promoting the corrosion resistance, in agreement with our observations from passsivation experiments [18].

5. Conclusions

STM combined with *in situ* XPS was applied to investigate the initial stages of oxidation and the growth mechanisms of the surface oxide at RT on a model austenitic SS surface, Fe-18Cr-13Ni(100), exposed to gaseous oxygen at ultra-low pressure.

Starting from the oxide-free surface, local supply of metallic Fe and Cr for oxide nucleation and growth is concluded to be at the origin of surface heterogeneity developed in the oxide grown at saturation. Fe oxide nucleation is preferential in the initial stages of reaction (for exposures below 3 L) owing to low reaction probability with Cr and a kinetic barrier effect of N-bonding on the otherwise favored oxidation of Cr. Nucleation of Fe oxide occurs at and in the vicinity of the periodic vacancy defect lines on the terraces and at terrace borders of the initial surface while Cr^{3+} oxide nucleation at the multi-steps is delayed to exposures of 3−6 L. Beyond 3 L, oxide nuclei grow to grain size of up to 2−3 nm and in

density until saturation of the surface by a nanogranular film homogeneously covering the substrate terraces and multi-steps. Oxide nuclei and nanograins develop no well-ordered structure, unlike at higher temperature (250 °C) where crystalline films are formed. A Cr-rich oxide film is formed at saturation with a Cr^{3+} to $Fe^{2+/3+}$ balance depending on the local supply of metallic Cr and Fe during nucleation and growth and resulting in compositional heterogeneity at the nanoscale of the granular morphology.

Compared to results obtained at 250 °C under almost the same ultra-low pressure exposure oxidation conditions and to the air-formed native film, the mechanisms of early oxidation observed in the present work at RT provide new insight for the preparation of well-structured and compact Cr-enriched oxide film as optimized barrier for corrosion protection, by adjusting the oxidation temperature and exposure conditions which are key parameters for tuning the surface composition and nanoscale morphology.

Acknowledgments

This project has received funding from the European Research Council (ERC) under the European Union's Horizon 2020 research and innovation program (ERC Advanced Grant No. 741123). Région Île-de-France is acknowledged for partial funding of the equipment.

Data availability

The data that support the findings of this study are available from the corresponding authors upon reasonable request.

References

[1] D. Macdonald, Passivity - The key to our metals-based civilization, Pure and Applied Chemistry 71 (1999) 951 – 978.

[2] C. O. A. Olsson, D. Landolt, Passive films on stainless steels - Chemistry, structure and growth, Electrochimica Acta 48 (2003) 1093–1104.

[3] H.-H. Strehblow, V. Maurice, P. Marcus, Passivity of metals, in: P. Marcus (Ed.), in: Corrosion Mechanisms in Theory and Practice, third edition, Taylor and Francis, CRC Press, 2011, pp. 235–326.

[4] P. Marcus, V. Maurice, Oxide Passive Films and Corrosion Protection, in: G. Pacchioni, S. Valeri (Eds.), Science and Technology, Wiley-VCH Verlag GmbH & Co. KGaA, Weinheim, 2012, pp. 119–144.

[5] V. Maurice, P. Marcus, Progress in corrosion science at atomic and nanometric scales, Progress in Materials Science 95 (2018) 132–171.

[6] H.-H. Strehblow, Passivity of metals studied by surface analytical methods, a review, Electrochimica Acta 212 (2016) 630–648.

[7] J. Castle, J. Qiu, A co-ordinated study of the passivation of alloy steels by plasma source mass spectrometry and x-ray photoelectron spectroscopy—1. characterization of the passive film, Corrosion Science 29 (5) (1989) 591–603.

[8] A. Pardo, M. Merino, A. Coy, F. Viejo, R. Arrabal, E. Matykina, Effect of Mo and Mn additions on the corrosion behaviour of AISI 304 and 316 stainless steels in H_2SO_4, Corrosion Science 50 (3) (2008) 780–794.

[9] G. Ilevbare, G. Burstein, The role of alloyed molybdenum in the inhibition of pitting corrosion in stainless steels, Corrosion Science 43 (3) (2001) 485–513.

[10] A. Greeff, C. Louw, H. Swart, The oxidation of industrial FeCrMo steel, Corrosion Science 42 (10) (2000) 1725 – 1740.

[11] V. Maurice, H. Peng, L. H. Klein, A. Seyeux, S. Zanna, P. Marcus, Effects of molybdenum on the composition and nanoscale morphology of passivated austenitic stainless steel surfaces, Faraday Discussion 180 (2015) 151–170.

[12] Z. Wang, E.-M. Paschalidou, A. Seyeux, S. Zanna, V. Maurice, P. Marcus, Mechanisms of Cr and Mo enrichments in the passive oxide film on 316l austenitic stainless steel, Frontiers in Materials 6 (2019) 232.

[13] B. Lynch, Z. Wang, L. Ma, E.-M. Paschalidou, F. Wiame, V. Maurice, P. Marcus, Passivation-induced Cr and Mo enrichments of 316l stainless steel surfaces and effects of controlled pre-oxidation, Journal of The Electrochemical Society 167 (2020) 141509.

[14] T. Massoud, V. Maurice, L. H. Klein, A. Seyeux, P. Marcus, Nanostructure and local properties of oxide layers grown on stainless steel in simulated pressurized water reactor environment, Corrosion Science 84 (2014) 198–203.

[15] V. Maurice, P. Marcus, Current developments of nanoscale insight into corrosion protection by passive oxide films, Current Opinion in Solid State and Materials Science 22 (4) (2018) 156 – 167.

[16] L. Ma, F. Wiame, V. Maurice, P. Marcus, Origin of nanoscale heterogeneity in the surface oxide film protecting stainless steel against corrosion, npj Materials Degradation 3 (29) (2019) 1–9.

[17] L. Ma, F. Wiame, V. Maurice, P. Marcus, New insight on early oxidation stages of austenitic stainless

steel from in situ XPS analysis on single-crystalline Fe-18Cr-13Ni(100), Corrosion Science 140 (2018) 205–216.

[18] L. Ma, E.-M. Pascalidou, F. Wiame, S. Zanna, V. Maurice, P. Marcus, Passivation mechanisms and pre-oxidation effects on model surfaces of FeCrNi austenitic stainless steel, Corrosion Science 167 (2020) 108483.

[19] V. Maurice, W. P. Yang, P. Marcus, X-ray photoelectron spectroscopy and scanning tunneling microscopy study of passive films formed on (100) Fe-18Cr-13Ni single-crystal surfaces, Journal of the Electrochemical Society 145 (3) (1998) 909–920.

[20] M. Lampimäki, K. Lahtonen, P. Jussila, M. Hirsimäki, M. Valden, Morphology and composition of nanoscale surface oxides on Fe-20Cr-18Ni(111) austenitic stainless steel, Journal of Electron Spectroscopy and Related Phenomena 154 (3) (2007) 69–78.

[21] C. Müller, C. Uebing, M. Kottcke, C. Rath, L. Hammer, K. Heinz, The structure of the surface compound CrN formed by cosegregation on a Fe-15Cr-N(100) single crystal surface, Surface Science 400 (1–3) (1998) 87 – 94.

[22] D. A. Harrington, A. Wieckowski, S. D. Rosasco, B. C. Schardt, G. N. Salaita, A. T. Hubbard, J. B. Lumsden, Films formed on well-defined stainless steel single-crystal surfaces in oxygen and water: studies of the (111) plane by LEED, auger and XPS, Corrosion Science 25 (10) (1985) 849 – 869.

[23] H. Fujiyoshi, T. Matsui, J. Yuhara, Segregation and morphology on the surface of ferritic stainless steel (001), Applied Surface Science 258 (19) (2012) 7664–7667.

[24] L. Ma, F. Wiame, V. Maurice, P. Marcus, Stainless steel surface structure and initial oxidation at nanometric and atomic scales, Applied Surface Science 494 (2) (2019) 8–12.

[25] CasaXPS, www.casaxps.com.

[26] SPIP, Scanning probe image processor, https://www.imagemet.com/products/spip/.

[27] P. Jussila, K. Lahtonen, M. Lampimäki, M. Hirsimäki, M. Valden, Influence of minor alloying elements on the initial stages of oxidation of austenitic stainless steel materials, Surface and Interface Analysis 40 (8) (2008) 1149–1156.

[28] J.-C. Dupin, D. Gonbeau, P. Vinatier, A. Levasseur, Systematic XPS studies of metal oxides, hydroxides and peroxides, Physical Chemistry Chemical Physics 2 (2000) 1319–1324.